Aerosol Science and Technology

ISSN: 0278-6826 (Print) 1521-7388 (Online) Journal homepage: www.tandfonline.com/journals/uast20

Deposition patterns of nanoparticles in a small S/W ratio impactor: measurements and physics

S. Kala & J. R. Saylor

To cite this article: S. Kala & J. R. Saylor (30 Jan 2026): Deposition patterns of nanoparticles in a small S/W ratio impactor: measurements and physics, Aerosol Science and Technology, DOI: 10.1080/02786826.2026.2618191

To link to this article: https://doi.org/10.1080/02786826.2026.2618191

AEROSOL SCIENCE AND TECHNOLOGY
https://doi.org/10.1080/02786826.2026.2618191

Deposition patterns of nanoparticles in a small S/W ratio impactor: measurements and physics

S. Kala and J. R. Saylor

Department of Mechanical Engineering, Clemson University, Clemson, South Carolina, USA

ABSTRACT

The deposition pattern for an impactor with a small nozzle-to-plate ratio (S/W) is a ring whose diameter is related to the particle diameter, among other quantities. The extant literature on impactors has focused on devices where S/W is of order unity and what literature exists for small S/W impactors has focused on micron-scale particles. Herein deposition patterns were obtained for particles ranging in diameter from 50 nm to 3 μm using scanning electron microscopy (SEM) where S/W was 0.09. Particle trajectory simulations mimicking the experimental conditions were also conducted to reveal the underlying physics. These showed the important role of the Hamaker constant, A and the coefficient of restitution, e as well as the importance of bounce, particle interception, and inertial effects (notwithstanding the small size of the particles considered). An improved relationship between the ring diameter and particle diameter is presented, and the relevance of this work to potential improvements in the diameter resolution of impactors is discussed.

GRAPHICAL ABSTRACT

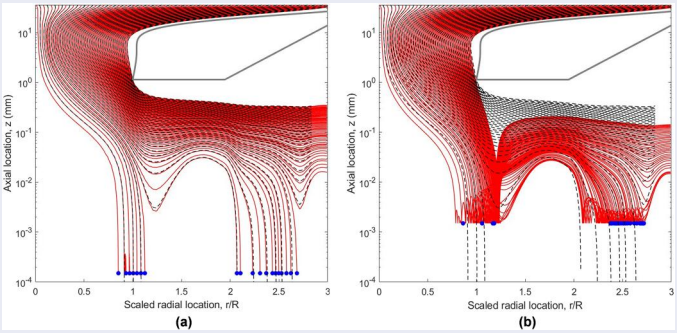

ARTICLE HISTORY
Received 3 July 2025
Accepted 6 January 2026

EDITOR
Coty Jen

1. Introduction

Accurate measurement of nanoparticles is critical to aerosol science. Many sophisticated methods for sizing and counting nanoparticles exist, such as electrical mobility spectrometry, dynamic light scattering, and small angle X-ray scattering to name a few. These approaches can be complex and expensive. Cascade impactors, on the other hand, can measure nanoparticles at a relatively low cost and are field deployable. A typical cascade impactor consists of a series of nozzle-and-plate combinations, stacked one over the other inside a cylindrical shell. The nozzle is oriented normally to the plate and the distance between the nozzle and plate is typically the same as the nozzle diameter. The air sample passes through the first stage where particles that are large and have sufficient inertia deposit on the plate while smaller particles move on to subsequent stages, each stage having a progressively smaller cutoff diameter. Gravimetric analysis of the particles collected at each stage is used to determine the particle size distribution, usually displayed as a histogram.

Since the development of the first cascade impactor in 1945 (May 1945), impactors have progressively improved (Kulkarni, Baron, and Willeke 2011; Le and Tsai 2021), and there is a rich body of literature on approaches taken to increase the resolution of impactors and to reduce the minimum detectable diameter of such impactors. For example, it has been

CONTACT J. R. Saylor jsaylor@clemson.edu Department of Mechanical Engineering, Clemson University, Clemson, SC 29634-0921, USA.
Supplemental data for this article can be accessed online at https://doi.org/10.1080/02786826.2026.2618191.

demonstrated that inclusion of an outer sheath of aerosol-free air surrounding the particle-laden jet significantly increases size resolution and that fine differential particle spectra can be obtained with two such impactors run in tandem, but with slightly different particle size cuts (Rao, Fernandez De La Mora, and McMurry 1992). A study by Fernandez De La Mora and Riesco-Chueca (1988) showed that the use of aerodynamic focusing of the particle stream (a technique discovered by Israel and Friedlander (1967) and further advanced by others (Fernandez de la Mora and Rosell-Llompart 1989; Rao, Navascues, and Fernandez De La Mora 1993; Fuerstenau, Gomez, and Fernandez De La Mora 1994)) increases sizing resolution yet further (Fernandez De La Mora 1996). The desire to measure particles of ever decreasing diameter has also resulted in improved impactor designs. Two general approaches to facilitating particle sizing measurements in the nanoscale region have been used: low-pressure impactors and micro-orifice impactors (Vanderpool, Lundgren, and Kerch 1990). The former reduces the mean free path of the air molecules, allowing very small particles to travel further and be collected on an impactor plate. Micro-orifice impactors utilize a large number of small jets (as opposed to one), enabling a very small diameter cutoff without the attendant loss of sample size that would occur for a single small jet. Low-pressure impactors have been developed by several groups (Hering, Flagan, and Friedlander 1978; Hering et al. 1979; Vanderpool, Lundgren, and Kerch 1990; Arffman, et al. 2014), and improved sensitivity of a low-pressure impactor *via* real time electrical detection of particles was obtained by Keskinen, Pietarinen, and Lehtimäki (1992) termed the electrical low-pressure impactor (ELPI) which was further refined to create the ELPI+ (Järvinen et al. 2014). The high-resolution low-pressure cascade impactor (HRLPI) has a cut point of 7.7 nm (Arffman, et al. 2014). The microorifice uniform deposit impactor (MOUDI) utilizes as many as 2000 nozzles as small as 52 μm to give a minimum particle sizing capability of 56 nm (Marple, Rubow, and Behm 1991), and down to 10 nm for its commercial implementation, the nanoMOUDI (MSP Corporation).

In addition to work on increasing particle size resolution and minimum detectable particle diameter, there have also been improvements in other aspects of impactor design including, control of particle bounce (McFarland, Ortiz, and Bertch 1978; Turner and Hering 1987; Tsai and Cheng 1995), reduction of particle loss (Fang, Marple, and Rubow 1991; Heo, et al. 2018), improved nanoparticle measurement capability in the workplace (Tsai, et al. 2012), use of particle charge (De Juan, et al. 1997; Marjamäki et al. 2000), and reduction in particle overloading (Turner and Hering 1987; Marple, Rubow, and Behm 1991; Huang, Tsai, and Shih 2001). However, a typical cascade impactor has six to ten stages, limiting the number of bins in the particle size distribution obtainable at any given moment to this same value.

The work described above concerned impactors where the nozzle-to-plate distance, S is one nozzle diameter, W, i.e., $S/W \sim O(1)$. For these conditions, the particle deposition pattern is a disk roughly the size of the nozzle diameter. There has been very little work on impactors where S/W is small, though what work has been conducted shows interesting behavior. Fredericks and Saylor (2018) showed that when $S/W \sim O(0.01)$, the particle deposition pattern is a fine ring and the diameter of that ring D is a function of the particle diameter d. Specifically, they observed that for $S/W = 0.047$ and $d = 3$ to 15 µm, D decreases with d in a single-stage impactor. This suggested the possibility of measuring multiple particle diameters within a single impactor stage, potentially increasing the number of bins in a particle size distribution that can be obtained from a given cascade design. This idea was further explored by Kala and Saylor (2022) who found that D is not only a function of d but also depends on S/W. Specifically, they observed that for $S/W = 0.03$ to 0.09 and $d = 2.7$ to 10 µm, D decreases with d and increases with S/W according to:

$$D_s = \frac{1.05(Stk) + 0.17(S/W) - 0.006}{Stk} \tag{1}$$

where $D_s = D/W$ and:

$$Stk = \frac{\rho u d^2}{9\mu W} \tag{2}$$

where ρ is the particle density, μ is the viscosity of air, and u is the nozzle exit velocity. The work of Fredericks and Saylor (2018) and Kala and Saylor (2022) explored particle diameters in the $d = 2.7$ to 10 µm range. A logical next step in exploring low S/W impactors is to ascertain the behavior of low S/W impactors in the nanometer range. The present study does precisely this, exploring the performance of a low S/W impactor for particle diameters ranging from 50 nm to 3 µm. Though the initial hope was that the resulting ring diameter would be sensitive to particle diameter as for the micron range, particle sizing resolution was in fact poor. However, several facets of low S/W impactor performance were identified which may

in the long-term lead to designs that will enable multiple particle size measurement on a single impactor stage at a single time interval. Also the deposition patterns differed from the micron scale, and aspects of the air flow were identified that may lead to improved impactor designs, as will be discussed.

Experiments were performed for $d = 50\,\text{nm}$ to $3\,\mu\text{m}$ ($Stk = 0.00001$ to 0.03). A value of $S/W = 0.09$ was chosen for this study, because this is where the highest resolution of d was observed by Kala and Saylor (2022). Particle deposition patterns were characterized using scanning electron microscopy (SEM), and the resulting particle surface density patterns are explained using particle trajectory simulations. We note that notwithstanding the small Stk explored here, as will be shown later, inertia plays a role in the particle deposition patterns observed.

This work also explores the conditions where maximum dispersion of particle diameters can be obtained in a single impactor stage, something of importance for future developments of impactors with higher diameter resolution. In our earlier work, and in a typical impactor setup, the sample stream expands through the entire nozzle plenum. And, for the experimental work presented here, that same approach is taken. However, in the simulations presented herein, the introduction of the sample at specific radial locations in the plenum is also explored, and the range of radial starting locations is ascertained that leads to maximum separation of particle diameters on the impaction surface.

2. Experimental method

The experimental setup is presented in Figure 1. Particle deposition patterns were explored for a range of Stk in a single-stage impactor. Radial particle surface density plots were obtained by passing monodisperse particles through the circular impactor nozzle and collecting them on a flat surface as shown in Figure 1. SEM images of the impaction surface were then obtained and used to obtain plots of particle count per unit area as a function of radius. These radial particle surface density profiles were then matched to those obtained from particle trajectory simulations to explain the mechanism of particle deposition that created the experimental profiles.

Nine particle diameters d were studied as listed in Table 1, with S/W set to 0.09. Polystyrene latex (PSL) spheres were chosen because of their availability in a wide range of diameters, their monodispersity, and their ease of aerosolization using an atomizer. For each run, 0.02 ml of the aqueous PSL solution (Thermo Scientific Nanosphere and Thermo Scientific DUKE Standard Microsphere) having a concentration of $C = 0.01$ gm PSL/ml were dissolved in 100 ml water before feeding the solution to the atomizer (TSI Model 9302). The entire 100 ml of solution was used during each run. Accordingly, the number of particles generated and used during each run was

Table 1. PSL particle diameters d, stokes numbers Stk, and number of PSL particles in the feed solution N_g for the nine cases performed.

d (nm)	Stk	N_g (count)
50	0.00001	2.8×10^{12}
100	0.00003	3.5×10^{11}
300	0.0003	1.3×10^{10}
500	0.0008	2.8×10^{9}
700	0.002	1.0×10^{9}
900	0.003	4.8×10^{8}
1100	0.004	2.6×10^{8}
1600	0.008	8.5×10^{7}
3000	0.03	1.3×10^{7}

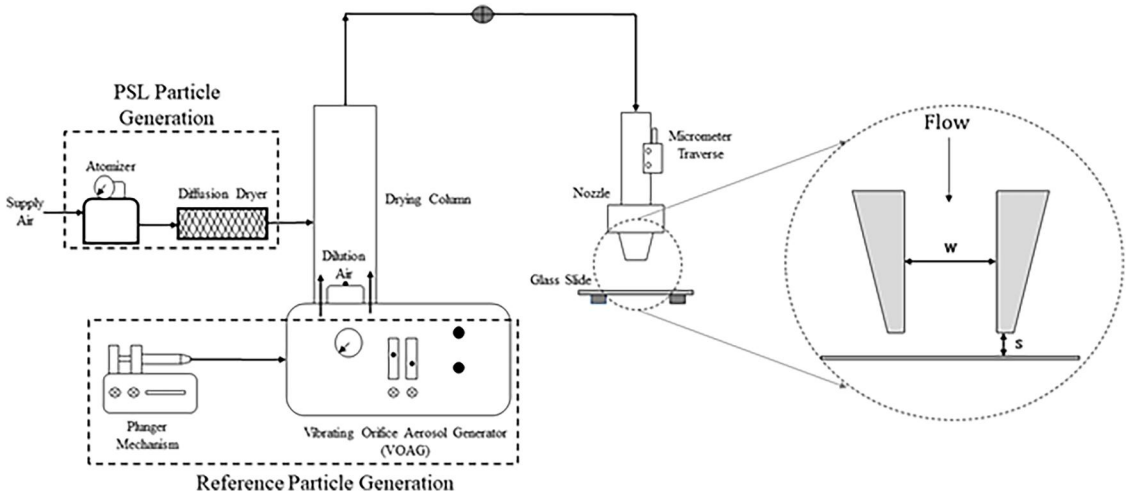

Figure 1. Schematic diagram of experimental setup.

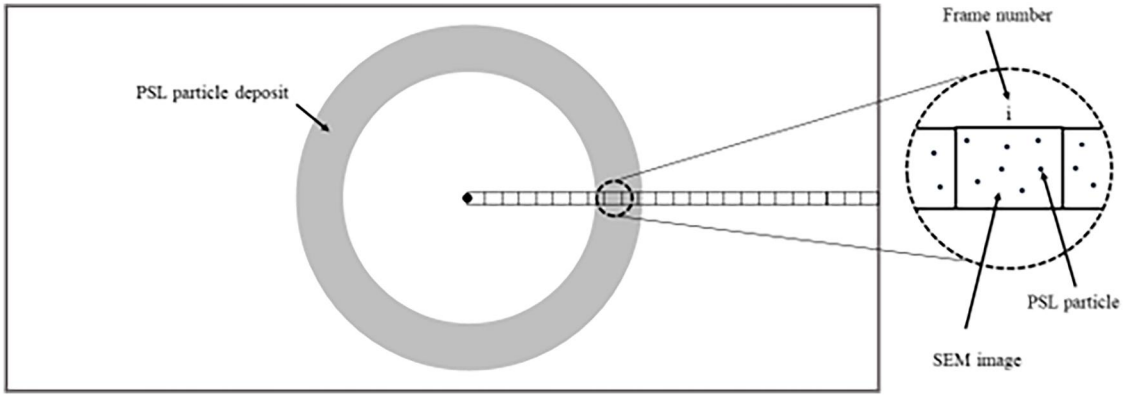

Figure 2. Schematic showing methodology for imaging PSL particle deposits. Note that the schematic is not to scale and that there were typically 40 to 100 image frames spanning the ring width.

$$N_g = \frac{m_s}{m_p} \tag{3}$$

where m_s is the mass of PSL in the aqueous solution (200 µg) and m_p is the mass of a single PSL particle obtained from the manufacturer's stated diameter and the density of PSL. Values of N_g for the nine *Stk* considered are presented in Table 1. The atomizer was a venturi device driven by laboratory compressed air.

The size of the liquid droplets generated by the atomizer is controlled by the inlet air pressure, which was set to 15 psi for the experiments presented here, resulting in droplets having a mean diameter of 3.5 µm. For each experimental run, particle deposition continued until the atomizer solution was exhausted, which typically took 60 min. A diffusion dryer was coupled to the atomizer outlet, drying the drops and leaving PSL particles. For an atomizer drop of 3.5 µm, the number of drops generated by the atomizer for 100 ml feed solution was 5×10^{12}, which exceeds the number of PSL particles in the feed solution for all nine test cases (*cf.* Table 1), ensuring there was <1 PSL particle in each drop, i.e., that doublets were not formed, something which was confirmed by the SEM images. The monodisperse particles were then passed through a vertical drying column of an aerosol generator (TSI Model 3450 VOAG - turned off during these runs) and carried by the dilution air at 50 lpm, to the impactor nozzle. The nozzle exit velocity was 6.6 m/s for all runs. The dilution air was charge neutralized by passing it through a Kr-85 neutralizer (TSI Model 3077 A) before entering the drying column.

The impactor nozzle used here was the same as that used in our prior work (Fredericks and Saylor 2018; Kala and Saylor 2022, 2023) and details of its construction can be found there. The nozzle was vertically mounted on a micrometer traverse to allow accurate setting of S/W. The impaction plates were $2'' \times 1''$ glass slides. Each glass slide was mounted on an optical lens holder which was fixed to a six-axis micrometer stage which was used to ensure that the plate was oriented perpendicular to the nozzle axis.

Before SEM imaging (Hitachi Regulus 8250 SEM), the slides were sputter coated (Ladd/Hummer^{TM} 6.2) with a thin conducting film of platinum to allow reflection of the SEM electron beam. For each slide, a line of images was obtained from the center of the ring to the edge of the deposition region. These images were separated by exactly one frame so that there was no overlap, nor gaps between images. For a given *Stk* case, imaging was performed at fixed magnification so that the area imaged in each frame was fixed. A schematic (not to scale) of the imaging methodology is shown in Figure 2. The SEM magnification varied with particle diameter to maintain visibility of particles in the frame. Accordingly, the number of frames comprising each radial sequence ranged from 3601 frames for the 50 nm case to 132 frames for the 3 µm case. This gives a frame area ranging from 30 µm^2 to 48,431 µm^2 for the 50 nm case and the 3 µm case, respectively. The images were processed in the MATLAB programming environment. Each image was binarized using the Bradley Method (Bradley and Roth 2007) which calculates the local mean intensity in the neighborhood of each pixel and sets the pixel to either black or white based on a locally adaptive threshold. Once the image was binarized, the area of connected pixels was determined and used to compute diameter. The particle count in each frame was used to obtain radial profiles of particle surface density, N in units of count/µm^2. This particle surface density N was then scaled to the maximum density N_m for each run to give a scaled particle number density, $N_s = N/N_m$. The number of bins used in the radial direction was computed using the square root method

wherein the number of bins was set to the square root of the number of frames, rounded off to the nearest integer (Davies and Goldsmith 1980).

The process described above required determination of the geometric center of the deposition rings prior to SEM imaging. To achieve this, disodium fluorescein (DSF) particles of diameter 15 µm, generated using a VOAG were passed through the single-stage impactor at $S/W = 1$. The DSF particles formed circular deposits which were denser and easier to see in the SEM images and were used to find the deposition center. Particles having diameters close to those of the DSF particles were rejected by the image analysis code, ensuring that DSF particles were not included in the PSL counts.

3. Simulation method

Since visualization of particle trajectories is not experimentally feasible due to the small particle diameters and confined geometry of the setup used here, the processes that led to the observed deposition patterns could not be determined experimentally. Accordingly, we conducted simulations to ascertain the trajectories and particle dynamics that resulted in the observed patterns. These simulations follow the same procedure as in our earlier work (Kala and Saylor 2023), and the reader is referred there for details; a summary of the approach is presented below.

The gas flow through the nozzle and impactor setup was simulated in ANSYS Fluent assuming symmetry about the nozzle axis, using the exact dimensions of the nozzle from the experiments, and using the same S/W. The velocity at the nozzle plenum was set to 0.55 m/s and with zero radial velocity, the same as for the experiments, and the nozzle exit velocity was 6.6 m/s as for the experiments, giving a nozzle Reynolds number of $Re = 5400$, which was obtained with a plenum-to-exit pressure drop of $\Delta p = 0.25$ psi (1720 Pa). The two-dimensional flow field was computed using a steady state pressure-based solver and viscous-laminar model. A mesh sensitivity analysis was conducted to ensure that the mesh size was sufficiently small to resolve the particle trajectories. Specifically, the trajectory of a 50 nm particle was obtained using the trajectory simulation code described below and the resulting deposition location was recorded as a function of mesh size. The analysis demonstrated convergence for mesh elements less than 90 nm, which was used in the simulations presented herein. The results of this mesh sensitivity study are presented in Figure S1 of the online supplemental information (SI).

Once the velocity field V was obtained, particle trajectories were simulated by integrating the particle force balance:

$$m\frac{dV_p}{dt} = F_d + F_g \tag{4}$$

where m is particle mass, V_p is particle velocity, F_d is drag force, dependent on the relative velocity of the particle $V_r = V - V_p$, and F_g is the gravitational force. A time step of 10^{-6} s was used. Impact was defined to occur when the particle center was less than or equal to one half diameter from the impaction surface. Whether the particle deposited or bounced upon impact was determined by comparing the normal incident velocity of the particle to the critical velocity for bounce v_c:

$$v_c = \left(\frac{(1-e^2)Ad}{6mz_0e^2}\right)^{1/2} \tag{5}$$

Here e is the normal coefficient of restitution, the ratio of normal rebound velocity of the particle to the normal incident velocity of the particle, A is the Hamaker constant which quantifies the adhesion energy, and z_0 is the equilibrium separation distance between the particle and surface which is assumed to be 0.2 nm (Israelachvili 1992). If the normal incident velocity of the particle was less than v_c, particle deposition occurred, otherwise the particle rebounded with a normal velocity equal to:

$$v_r = \left(e^2 - (1-e^2)\frac{Ad}{6mz_0{v_{n,i}}^2}\right)^{1/2} v_{n,i} \tag{6}$$

This resulting rebound velocity (using a conserved tangential velocity to complete the vector) was then used in Equation (4) and computation of the particle trajectory continued. Once the fate of all particles was determined, the resulting radial profiles for N were computed, binned, and scaled to give $N_s = N/N_m$, as for the experimental data, enabling comparison with the experimental plots. The number of bins for distributing N_s was computed using the square root method wherein the number of bins were taken as the square root of the total number of the particle trajectories simulated for each particle diameter which was 2151, rounded off to the nearest integer.

Equations (5) and (6) require values for A and e. For the PSL-glass combination A was obtained using the Lifshitz theory (Lifshitz 1956) which takes into account the bulk material properties, namely the optical properties of the material over the complete

electromagnetic spectrum (Visser 1972). Using this approach, A for interaction between medium 1 and medium 2 across medium 3 is given by:

$$A \cong \frac{3}{4}k_B T\left(\frac{\varepsilon_1-\varepsilon_3}{\varepsilon_1+\varepsilon_3}\frac{\varepsilon_2-\varepsilon_3}{\varepsilon_2+\varepsilon_3}\right) + \frac{3h\nu_e}{8\sqrt{2}}\left(\frac{(n_1{}^2-n_3{}^2)(n_2{}^2-n_3{}^2)}{\sqrt{n_1{}^2+n_3{}^2}\sqrt{n_2{}^2+n_3{}^2}(\sqrt{n_1{}^2+n_3{}^2}+\sqrt{n_2{}^2+n_3{}^2})}\right) \quad (7)$$

where k_B is the Boltzmann constant, T is temperature, ε_i is the dielectric constant of the material, h is Planck's constant, n_i is the refractive index of the material in the visible range, and ν_e is the electronic absorption frequency in the ultraviolet (Lifshitz 1956). Equation (7) assumes the absorption frequencies of all three interacting media is the same (Lifshitz 1956). Equation (7) gives $A = 8 \times 10^{-20}$ J for a PSL particle interacting with glass in air.

Given the lack of information for e for PSL particles impacting glass substrates at different Stk, an iterative approach was used where e was varied until the resulting plot of N_s versus r/R for the simulations agreed with the experimental plot. For each particle diameter 2151 particle trajectories were simulated. The trajectory starting points were placed at equal separation of 0.01 mm from each other at the nozzle inlet starting at $r = 0.1$ mm and moving radially outward toward the nozzle wall. For each e an N_s versus r/R plot was obtained (where R is the nozzle radius), and four characteristics were computed: inner peak location (R_1), outer peak location (R_2), inner peak amplitude (H_1) and outer peak amplitude (H_2). These four characteristics of the N_s versus r/R plots were compared to the corresponding values of their experimental counterparts. An example is shown in Figure 3. The degree of agreement between the simulation and experiment was quantified by the sum of the square of the differences of the four characteristics:

$$\sigma = (R_1 - R_{1,s})^2 + (R_2 - R_{2,s})^2 + (H_1 - H_{1,s})^2 + (H_2 - H_{2,s})^2 \quad (8)$$

where the subscript s denotes the value for the simulation. Values for σ were first computed for e ranging from 0 to 0.99 in increments of 0.1. Once a minimum in σ was determined for all nine cases, refined simulations were performed in the vicinity of the minima with e varied in progressively smaller increments. Figure 4 presents the variation of σ with 1-e. For each particle diameter, the value of e corresponding to the minimum σ was chosen. The resulting values of e increase with d, in agreement with previous research for micron-scale and sub-micron particles (Dahneke 1971, 1975; Gollwitzer et al. 2012) and are presented in Table 2. The numerical range of e for PSL particles agrees with Dahneke (1971, 1975).

When doing simulations of small particles, it is possible that Brownian motion, which wasn't considered in these simulations, could potentially affect the results. However, for the smallest particle considered here (50 nm), the characteristic diffusion length L is much larger than the ring structures observed or computed. This can be demonstrated using a characteristic diffusion length, $L = (D't)^{1/2}$ where D' is obtained

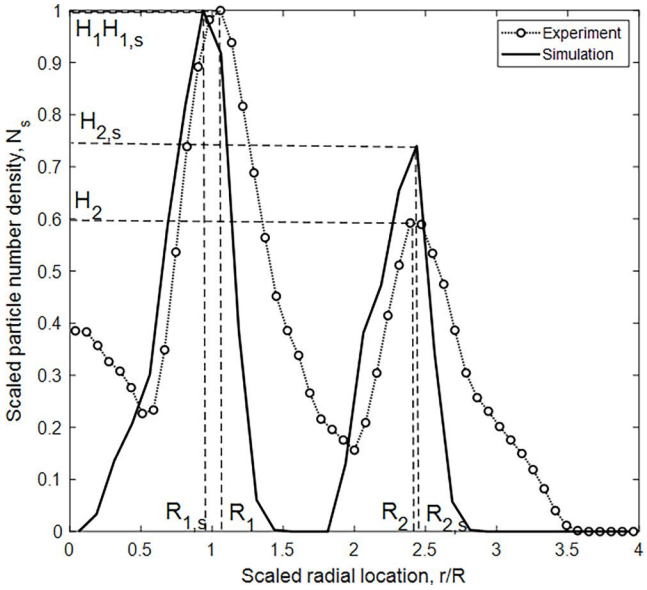

Figure 3. Plot of scaled particle surface density N_s versus scaled radial location r/R for the $Stk = 0.0003$ case, comparing the experiment and simulation using four characteristics: inner ring location (R_1), outer ring location (R_2), inner ring amplitude (H_1) and outer ring amplitude (H_2). The subscript "s" refers to the simulations.

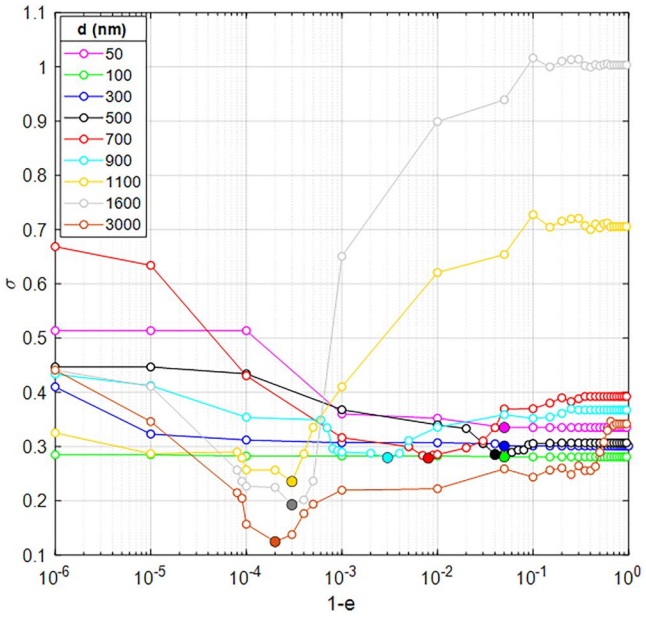

Figure 4. Plot of σ versus $1 - e$ for all nine particle diameters d.

Table 2. Coefficient of restitution (e) determined from simulation of particle trajectories.

d (nm)	Stk	e
50	0.00001	0.95
100	0.00003	0.95
300	0.0003	0.95
500	0.0008	0.96
700	0.002	0.992
900	0.003	0.997
1100	0.004	0.9997
1600	0.008	0.9997
3000	0.03	0.9998

from Einstein's equation for diffusivity of a particle in a gas, $D' = (R_g T)/(3\mu\ d\ N_a)$, where R_g is the gas constant, T temperature, μ the viscosity of air, N_a is Avogadro's number, and t is the residence time from the nozzle exit to the outer radius of the nozzle. Using these equations, one obtains $L = 2.8\,\mu m$. The ring structures we present here have separations and FWHM on the order of millimeters, three orders of magnitude larger. So, though the rings we obtain *via* simulations would be slightly blurred by the presence of Brownian motion, this effect would be small.

4. Results and discussion

Figure 5 presents a plot of some of the experimental results on N_s versus r/R coordinates where R is the nozzle radius, $N_s = N/N_m$, and N_m is the maximum particle surface density for that run. To reduce clutter, Figure 5 presents data for just four cases, Stk = 0.0003, 0.002, 0.004, and 0.03. The interested reader can find the data for all nine Stk plotted on both N versus r/R coordinates and N_s versus r/R coordinates in the SI, Figures S2 and S3, respectively. A two-peak structure exists for virtually all Stk considered, corresponding to a two-ring deposition pattern. The N_s versus r/R profiles are presented for the same four Stk in Figure 6 with the experimental results and simulations superimposed, showing reasonable agreement, the simulations revealing the same two-ring behavior found in the experiments. The N_s versus r/R profiles for all nine Stokes numbers are presented in Figures S4 through S12 in the SI.

The diameter of the inner and outer rings, D_1 and D_2, respectively, are plotted against d in Figure 7, showing that both diameters decrease slightly with d (Stk) and showing good agreement between experiments and simulations. The amplitude of the inner and outer peaks, H_1 and H_2 are plotted against d in Figure 8 showing that $H_1 = 1$ for $d < 500\,nm$ and $H_2 = 1$ for $d > 500\,nm$ for both experiments and simulations. This means that the dominant ring, i.e., the ring with higher N_s, changes from the inner ring to the outer ring at $Stk \sim 0.001$ ($d = 500\,nm$). Both the experiments and the simulations show a decrease in the inner peak amplitude with Stk and an increase in the outer peak amplitude with Stk.

These results show that, in contrast to the case for microscale particles, for nanoparticles (and for $S/W \sim O(0.01)$), the particle deposition pattern changes from a single ring to a two-ring structure. Also, these results show that, in agreement with the case for

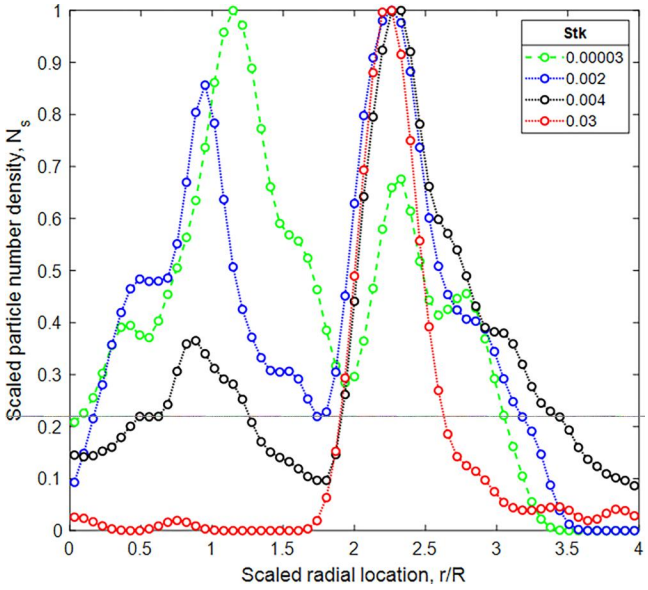

Figure 5. Plot of scaled particle surface density N_s versus scaled radial location r/R for four representative Stokes numbers.

microscale particles, for nanoparticles the diameters of both rings D_1 and D_2 decrease with *Stk*.

The replication of the essential characteristics of the rings in the simulations is significant since they take into account only inertial forces, interception, particle elasticity, and van der Waals adhesion forces and do not take into account any lift forces such as the Magnus or Saffman lift forces, suggesting that these forces do not contribute significantly to the observed behavior.

We now use the particle trajectory simulations to explain (i) why there are two rings, (ii) why the dominant ring changes from the inner to the outer as *Stk* increases, (iii) why the ring diameter changes with *Stk*, and (iv) how introduction of the air sample at specific nozzle plenum inlet locations could improve detectivity of d using D. These explanations are facilitated by the flow streamlines and particle trajectories presented in Figure 9, for the particle diameters d = 300 nm ($Stk = 0.0003$) in Figure 9a and d = 3 µm ($Stk = 0.03$) in Figure 9b. The salient feature of the flow field presented in Figure 9 is the separation bubble that exists from $r/R{\sim}1.2$ to $r/R{\sim}2$. It is noted that the z-axis in Figure 9 is logarithmic and that this separation bubble extends less than 100 µm into a channel flow that is 1 mm high. Nevertheless, this separation bubble explains much about the double ring structure.

The channel flow formed between the face of the nozzle and the impaction surface initially accelerates due to the favorable pressure gradient that forms radially outward from the stagnation point at $r/R = 0$. However, the face of the nozzle rises upward at $r/R \sim 2$, increasing the channel height, decreasing the flow velocity, and creating an adverse pressure gradient which causes the separation bubble that exists from $r/R \sim 1.2$ to $r/R \sim 2$. In this work, depositions occur by either interception or inertial deposition, and in the region of the separation bubble, neither can occur. The streamlines primarily flow above the 100 µm separation bubble, preventing interception with the surface for even the largest particle considered here, 3 µm. And since the streamlines above the separation bubble flow roughly horizontally, inertial deposition is not possible beneath the separation bubble. Hence, two rings form primarily because deposition is possible only before and after the separation bubble and not beneath the separation bubble. We note in passing that the channel geometry created by the plate and nozzle surfaces is not dissimilar from that presented in Cooper and Spielman (1974), though the Reynolds numbers are different; these authors do not note the existence of a separation bubble.

Figure 9 shows the trajectories and deposition behavior for two extreme particle diameters, 300 nm for Figure 9a and 3 µm for Figure 9b, revealing how and why these small/large particles deposit where they do. Figure 9a shows that the 300 nm particles follow the streamlines very closely, showing little deviation due to their small inertia. Hence, deposition in this case occurs almost exclusively by interception, though one of the trajectories shows bounce which causes the particle to deposit slightly outward of its initial contact point, however this is the exception proving the rule of deposition by interception for the smallest particles considered here. Largely, the deposition pattern

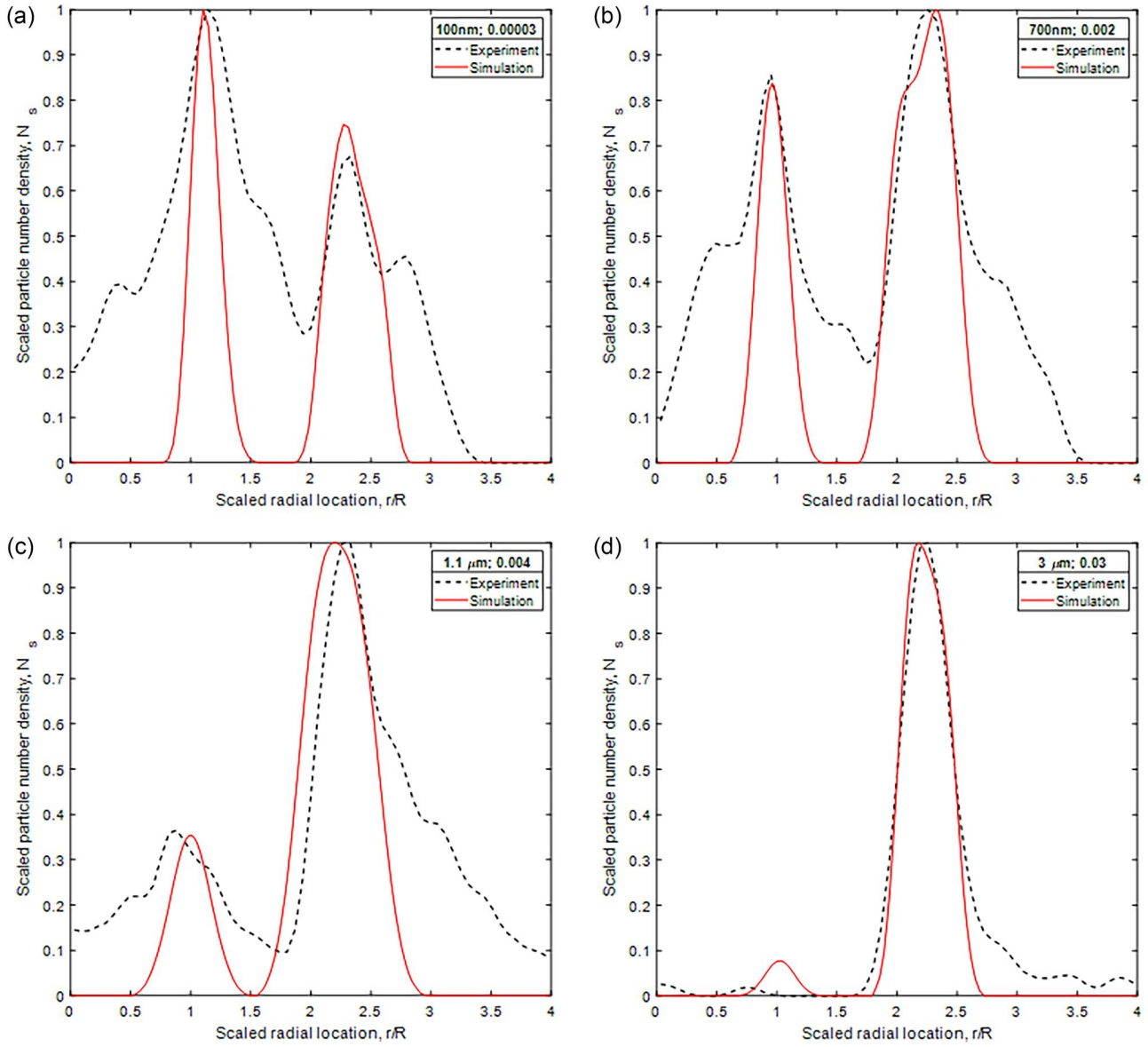

Figure 6. Plot of scaled particle surface density N_s versus scaled radial location r/R for (a) $Stk = 0.00003$, (b) $Stk = 0.002$, (c) $Stk = 0.004$, and (d) $Stk = 0.03$. The dashed line is the experimental N_s versus r/R plot. The solid line is the scaled particle surface density obtained from the simulations.

for the 300 nm particles is determined by the first location at which the streamline comes within $d/2$ of the surface (*viz.* 150 nm from the surface in this case). Particles that enter the nozzle plenum close to the axis, are transported by streamlines that come within $d/2$ of the surface at a radial location inside of the separation bubble. Conversely, particles that enter the nozzle plenum slightly farther from the axis are carried by streamlines that come within $d/2$ of the surface on the outer side of the separation bubble. This is the way the two rings form for smaller particles. It may be noted that the number of streamlines that approach the surface radially inward of the separation bubble is a relatively small fraction of the total number of streamlines. This might lead one to incorrectly conclude that for small particles, the outer ring, D_2 should have the large amplitude. However, this is not the case, and the reason that, for small particles, the inner ring has the larger amplitude (*cf.* Figure 6a) is that many of the particles that enter the nozzle plenum at large radial location do not deposit at all, flowing instead out of the domain, as can easily be seen on the right-hand side of Figure 9a. Hence, for small particles, the inner peak dominates, though this situation quickly reverses with larger particles for reasons that are now explained.

For the larger, $d = 3\,\mu$m particles presented in Figure 9b, significant deviation of the trajectories

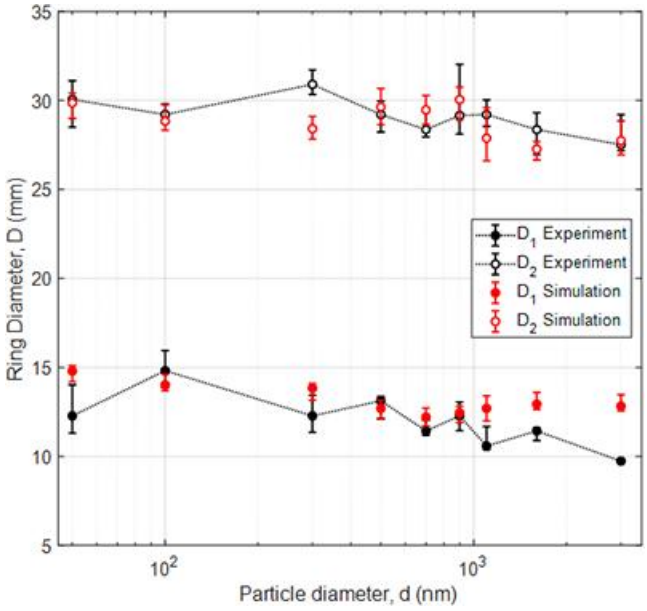

Figure 7. Comparison of experimental and simulation values of D_1 and D_2 for all nine *Stk* cases. The uncertainty in D is the full-width-half-max for the ring width in the N_s versus r/R plots.

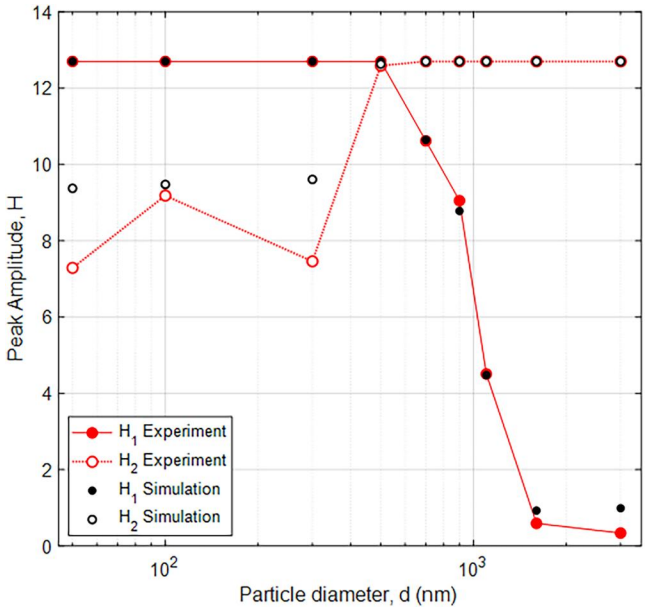

Figure 8. Comparison of experimental and simulation peak amplitude H versus particle diameter for all nine *Stk* cases. Here H_1 represents the amplitude N_s for the inner ring and H_2 represents the amplitude of N_s for the outer ring.

from the streamlines occurs, as expected. Also, in contradistinction from the smaller particles, particle bounce plays an important role in the trajectories of these larger particles. For the 3 µm particles whose trajectories start in the portion of the nozzle plenum close to the axis, their paths deviate from the streamlines, impact the surface in the vicinity of $r/R \sim 1$, bounce multiple times, and then deposit. However, few of these particles deposit in the region of the inner ring. Instead, they either bounce in the region of the inner ring and are then carried by the flow out and around the separation bubble where they deposit to form the second ring or bounce and flow out of the domain altogether. For the 3 µm particles whose trajectories start in the portion of the nozzle plenum far from the axis, their paths flow over the separation bubble, impact the surface and, after bouncing, either deposit or leave the domain. These two processes combined cause most of the particles that deposit in the 3 µm case to deposit in the outer ring. Stated another way, in contrast to the 300 nm particles, for the 3 µm case, contribution of deposition in the outer

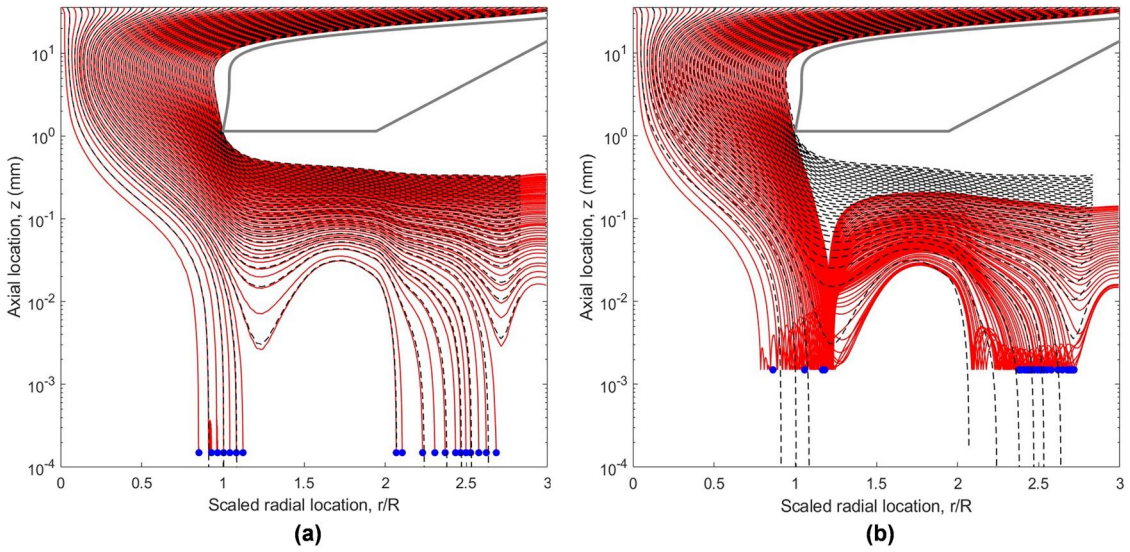

Figure 9. Particle trajectories for (a) $Stk = 0.0003$ ($d = 300$ nm) and (b) $Stk = 0.03$ ($d = 3$ µm). Each of these figures display 80 trajectories which start at equal separation of 0.25 mm from each other at the nozzle inlet beginning at $r = 0.05$ mm and moving radially outward. For both (a) and (b), the red lines are particle trajectories, the black dashed lines are the flow streamlines, and the blue dots represent the final deposition location of the trajectories. The solid gray line represents the nozzle contour. Since no trajectory can get closer than $d/2$ from the surface, the red trajectories end at two very different values of z, due to the two very different particle diameters presented in (a) and (b).

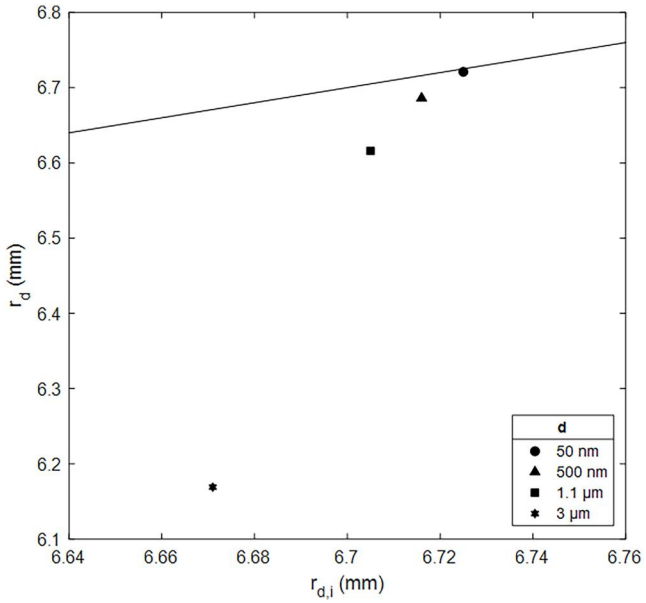

Figure 10. Comparison of actual radial deposition location r_d versus radial deposition location for a massless particle $r_{d,i}$ at a fixed radial starting location at nozzle plenum inlet $r_s = 2$ mm for four particle diameters 50 nm, 500 nm, 1.1 µm, and 3 µm. The black line is the line of unity slope.

ring occurs from particles whose streamlines begin both near the axis of the plenum (and which bounce from the inner ring region to the outer ring) and far from the axis, resulting in a dominant outer ring for larger particles, in accordance with Figures 6b–d.

Particle bounce increases with d and plays a more prominent role in determining the particle deposition pattern. Bounce increases with d because larger particles have greater inertia and a lower critical velocity v_c (v_c is inversely proportional to d^2 [Dahneke 1971; Wang and Kasper 1991; Weir and McGaving 2008]). Additionally, the coefficient of restitution e increases with d as shown in Figure 4 and Table 2. This causes larger particles to retain greater kinetic energy at bounce and undergo multiple bounces before depositing.

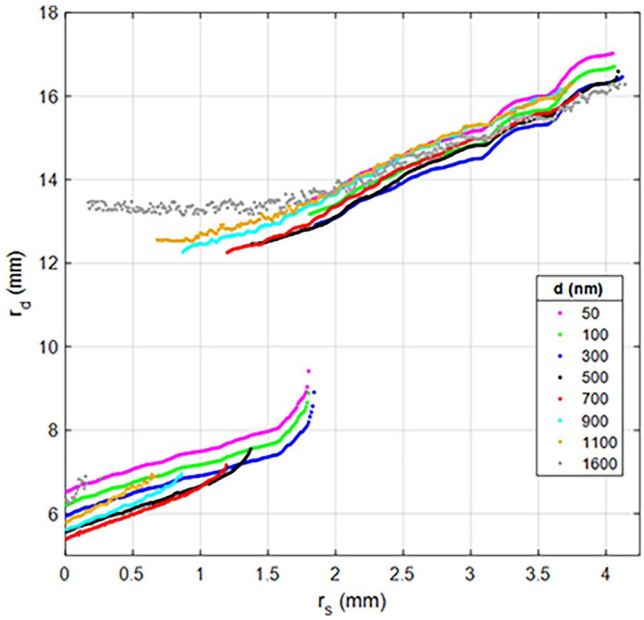

Figure 11. Plot of radial deposition location on the impactor surface r_d versus the radial starting location at the nozzle plenum inlet r_s.

It should be noted here that for small nanometer scale particles, deposition is dominated by interception and not inertia, but the deposition location still differs from that of a massless particle. This is quantified in Figure 10 where the actual deposition location is plotted against the deposition location of a massless particle (a particle with the same diameter, but no mass). The radial starting location in the nozzle plenum is $r_s = 2$ mm, and four particle diameters are presented: 50 nm, 500 nm, 1.1 µm, and 3 µm. This plot shows that the effect of inertia and adhesion forces decreases substantially for small particles but does not disappear completely for the diameters explored here.

As shown in Figure 7, both inner and outer ring diameters decrease with d. The explanation for this lies in the fact that regardless of whether inertia or interception dominates, both result in a smaller ring as d increases. For particles falling in the small d range, deposition is dominated by interception, and in this situation, the smaller the particle, the further outward the streamline must travel before coming within $d/2$ of the surface, resulting in a progressively larger ring diameter. For particles falling in the large d range, inertia dominates and causes particles to deviate from the outward motion of the streamline to deposit at an inner location, this effect increasing with d, and resulting in ring diameters that decrease with d.

But, the variation in D with d shown in Figure 7 is relatively weak, limiting the ability to detect multiple particle diameters with a single-stage impactor in the nanoscale range. However, the discussion presented above reveals that the ultimate location of particle deposition is determined in part by the starting radial location of the particle in the nozzle plenum. Hence, it is possible that by limiting the inlet radial location where an air sample is introduced might improve the D versus d behavior seen in Figure 7. This is explored in Figure 11 which is a plot of the radial deposition location r_d versus the radial starting location in the nozzle plenum r_s for all particle diameters considered here, showing that at certain r_s the dispersion in r_d over the particle diameters considered, is larger than for other r_s. This can be exploited to increase the change in ring diameter with particle diameter. To determine the optimum radial starting locations resulting in maximal separation in deposition location among the particle diameters considered, a resolution parameter is defined:

$$\Delta = \frac{D_a - D_b}{(d_a - d_b)} \tag{9}$$

where D is the ring diameter and d is the particle diameter, and a and b refer to two successive particle diameters. The average of Δ for nine particle diameters was calculated for radial starting locations intervals of 0.1 mm. The r_s interval that maximizes Δ is $r_s = 0.87$ mm − 0.97 mm which gives $\Delta = 4.7$ µm/nm. Using the same particle trajectory simulation methodology as above, 100 particle trajectories were simulated for each particle diameter, with radial starting locations r_s constrained to 0.87 mm to 0.97 mm and separated by 1 nm. The resulting N_s versus r/R plots

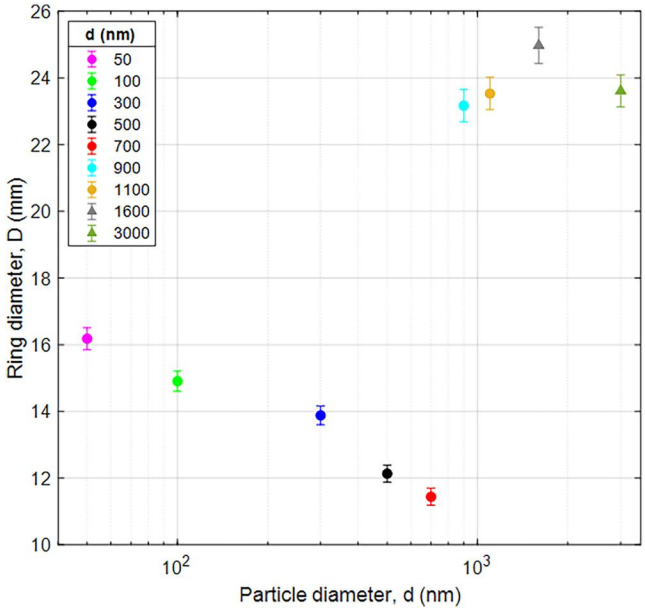

Figure 12. Plot of ring diameter D versus particle diameter d obtained from particle trajectory simulations for $r_s = 0.87$ mm to 0.97 mm where r_s is the radial starting location in the nozzle plenum. The error bars are the full width half max of the ring.

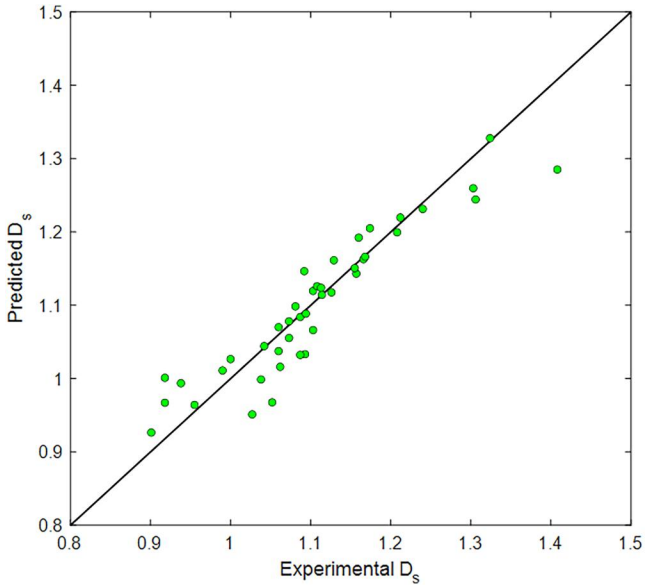

Figure 13. Plot of the experimental ring diameter versus that predicted by Equation (10). A line of unity slope is included.

were used to generate the D versus d plot presented in Figure 12 which shows much improved resolution for $d = 50$ nm to 700 nm particles than for Figure 7, and no overlap of the full-width-half-max rings. Based on this analysis, for particle diameter d ranging from 50 nm to 700 nm in a single-stage impactor, the ring separation is ~7 µm/nm and the average ring thickness (FWHM) for a monodisperse particle inlet is 0.55 mm, suggesting the potential to differentiate between particles with diameters that differ by 79 nm. The analysis does show poor resolution for 900 nm and 1.1 µm particles but the resolution improves for 1.6 µm and 3 µm particles. However, other methods perform better for these larger particles; it is in the tens and hundreds of nanometers where challenges lie.

The data from Figure 12 for particle diameters less than 900 nm were used to generate a fit to the data which is presented in Equation (10). The fit was obtained using the curve fitting tool in the MATLAB programming environment. Here A' is the Hamaker constant normalized to $1 \times 10^{-20} J$ and D_s is the ring

diameter D scaled to the nozzle width W:

$$D_s = 2.14\frac{(S/W)^{0.17}(e)^{0.22}}{(Stk)^{0.07}(A')^{0.21}} \quad (10)$$

Figure 13 is a plot of the predicted and actual D_s. Deviation from the unity slope line is small. The data from our previous studies are also incorporated in Figure 13. As expected, Equation (10) reveals that the ring diameter D increases with S/W and e, and decreases with Stk and A.

5. Conclusions

Experiments and particle trajectory simulations of particle impaction were conducted at $S/W = 0.09$ for particles in the nanometer diameter range. The decrease in particle diameter d and thus Stk from the micron-scale case leads to change in the deposition behavior from a single ring to a double ring for $d < 1\,\mu m$. This is due to a transition in the physics of deposition over the diameter range explored, namely a shift from inertially dominated impaction to interception dominated impacts. The diameter of the rings is a function of not just Stk and S/W but also depends on particle surface interaction quantified by A and particle elasticity, quantified by e. The results presented in this study allow the prediction of particle deposition patterns for a wide range of Stk and thus open further possibilities for using ring diameters D to predict the particle diameters d in inertial impactors thereby improving the overall resolution of particle size distributions using impactors, though further work is needed to demonstrate the practical feasibility of such an approach. The separation bubble in the flow plays an important role in the ring pattern, and this suggests that further improvements in this approach to particle sizing would benefit from a change in the face of the nozzle geometry to maximize the impact of the separation bubble on deposition location.

Nomenclature

A	Hamaker constant
A'	scaled Hamaker constant
C	particle mass density in solution
d	particle diameter
D	ring diameter
D_s	scaled ring diameter, D/W
D_1	diameter of inner ring
D_2	diameter of outer ring
D'	particle diffusion coefficient
e	normal coefficient of restitution
F_d	drag force
F_g	gravitational force
h	Planck's constant
H_1	amplitude of inner ring
H_2	amplitude of outer ring
k_B	Boltzmann constant
L	characteristic diffusion length
m	particle mass
m_s	mass of PSL in the aqueous solution
m_p	mass of a single PSL particle
n_i	refractive index
N	particle surface density on glass slide
N_a	Avogadro's number
N_g	number of particles generated in a run
N_m	maximum surface density
N_s	scaled surface density
P	pressure
r_d	radial deposition location
$r_{d,i}$	radial deposition location for massless particle
r_s	radial starting location
R	nozzle radius
Re	Reynolds number
R_g	ideal gas constant
Stk	Stokes number
T	temperature
u	nozzle exit velocity
v_c	critical bounce velocity
ν_e	electronic absorption frequency
$v_{n,i}$	normal incident velocity
v_r	rebound velocity
V	air velocity
V_p	particle velocity
V_r	velocity difference $V-V_p$
W	nozzle diameter
z_0	equilibrium separation distance
Δ	resolution parameter
ε_i	dielectric constant
μ	air viscosity
ρ	air density
σ	deviation of simulations from experiments

Disclosure statement

No potential conflict of interest was reported by the authors.

Funding

This material is based upon work supported by the National Science Foundation under Grant No. 1804304.

ORCID

S. Kala http://orcid.org/0000-0003-2824-6144

References

Arffman A et al. 2014. High-resolution low-pressure cascade impactor. J Aerosol Sci. 78:97–109. https://doi.org/10.1016/j.jaerosci.2014.08.006

Bradley D, Roth G. 2007. Adapting thresholding using the integral image. J Graphics Tools. 12(2):13–21. https://doi.org/10.1080/2151237x.2007.10129236

Cooper DW, Spielman LA. 1974. A new particle size classifier: variable-slit impactor with photo-counting. Atmos Environ. (1967). 8(3):221–232. https://doi.org/10.1016/0004-6981(74)90089-4

Dahneke B. 1971. The capture of aerosol particles by surfaces. J Colloid Interface Sci. 37(2):342–353. https://doi.org/10.1016/0021-9797(71)90302-x

Dahneke B. 1975. Further measurements of the bouncing of small latex spheres. J Colloid Interface Sci. 51(1):58–65. https://doi.org/10.1016/0021-9797(75)90083-1

Davies OL, Goldsmith PL. 1980. Statistical methods in research and production. Longman.

De Juan L et al. 1997. Electrostatic effects in inertial impactors. J Aerosol Sci. 28(6):1029–1048. https://doi.org/10.1016/s0021-8502(96)00490-9

Fang CP, Marple VA, Rubow KL. 1991. Influence of cross-flow on particle collection characteristics of multi-nozzle impactors. J Aerosol Sci. 22(4):403–415. https://doi.org/10.1016/0021-8502(91)90001-x

Fernandez De La Mora J, Riesco-Chueca P. 1988. Aerodynamic focusing of particles in a carrier gas. J Fluid Mech. 195:1–21.

Fernandez De La Mora J, Rosell-Llompart J. 1989. Aerodynamic focusing of heavy molecules in seeded supersonic jets. J Chem Phys. 91(4):2603–2615. https://doi.org/10.1063/1.456969

Fernandez De La Mora J. 1996. Drastic improvement of the resolution of aerosol size spectrometers via aerodynamic focusing: the case of variable-pressure impactors. Chem Eng Commun. 151(1):101–124.

Fredericks S, Saylor JR. 2018. Ring-shaped deposition patterns in small nozzle-to-plate distance impactors. Aerosol Sci. Technol. 52(1):30–37. https://doi.org/10.1080/02786826.2017.1377829

Fuerstenau S, Gomez A, Fernandez De La Mora J. 1994. Visualization of aerodynamically focused subsonic aerosol jets. J Aerosol Sci. 25(1):165–173. https://doi.org/10.1016/0021-8502(94)90188-0

Gollwitzer F, Rehberg I, Kruelle CA, Huang K. 2012. Coefficient of restitution for wet particle. Phys Rev E Stat Nonlinear Soft Matter Phys. 86(1 Pt 1):011303. https://doi.org/10.1103/PhysRevE.86.011303[23005407]

Hering SV, Flagan RC, Friedlander SK. 1978. Design and evaluation of new low-pressure impactor. 1. Environ Sci Technol. 12(6):667–673. https://doi.org/10.1021/es60142a004

Hering SV, Collins JJ, Friedlander SK, Richards LW. 1979. Design and evaluation of a new low-pressure impactor. 2. Environ Sci Technol. 13(2):184–188. https://doi.org/10.1021/es60150a009

Huang CH, Tsai CJ, Shih TS. 2001. Particle collection efficiency of an inertial impactor with porous metal substrates. J Aerosol Sci. 32(9):1035–1044. https://doi.org/10.1016/s0021-8502(01)00038-6

Heo JE et al. 2018. Effect of horizontal inlet on slit-nozzle virtual impactor performance. J Mech Sci Technol. 32(5):2419–2424. https://doi.org/10.1007/s12206-018-0454-8

Israel GW, Friedlander SK. 1967. High-speed beams of small particles. J Colloid Interface Sci. 24(3):330–337. https://doi.org/10.1016/0021-9797(67)90258-5

Israelachvili JN. 1992. Intermolecular and surface forces. Academic Press.

Järvinen A, Aitomaa M, Rostedt A, Keskinen J, Yli-Ojanperä J. 2014. Calibration of the new electrical low pressure impactor (ELPI+). J Aerosol Sci. 69:150–159. https://doi.org/10.1016/j.jaerosci.2013.12.006

Kala S, Saylor JR. 2022. Factors affecting the diameter of ring-shaped deposition patterns in inertial impactors having small S/W ratios. Aerosol Sci Technol. 56(3):234–246. https://doi.org/10.1080/02786826.2021.2007214

Kala S, Saylor JR. 2023. The effect of relative humidity on deposition pattern in inertial impactors: the role of particle elasticity and surface attraction. Powder Technol. 428:118798. https://doi.org/10.1016/j.powtec.2023.118798

Keskinen J, Pietarinen K, Lehtimäki M. 1992. Electrical low pressure impactor. J Aerosol Sci. 23(4):353–360. https://doi.org/10.1016/0021-8502(92)90004-f

Kulkarni P, Baron PA, Willeke K. 2011. Aerosol measurement: principles, techniques, and applications. Wiley.

Le TC, Tsai CJ. 2021. Inertial impaction technique for the classification of particulate matters and nanoparticles: a review. KONA. 38(0):42–63. https://doi.org/10.14356/kona.2021004

Lifshitz EM. 1956. Theory of molecular attractive forces between solids. J Exp Theor Phys (JETP). 2:73–83.

Marjamäki M, Keskinen J, Chen D-R, Pui DYH. 2000. Performance evaluation of the electrical low-pressure impactor (ELPI). J Aerosol Sci. 31(2):249–261. https://doi.org/10.1016/s0021-8502(99)00052-x

Marple VA, Rubow KL, Behm SM. 1991. A microorifice uniform deposit impactor (MOUDI): Description, calibration, and use. Aerosol Sci Technol. 14(4):434–446. https://doi.org/10.1080/02786829108959504

May KR. 1945. The cascade impactor: an instrument for sampling coarse aerosols. J Sci Instrum. 22(10):187–195. https://doi.org/10.1088/0950-7671/22/10/303

McFarland AR, Ortiz CA, Bertch RW Jr. 1978. Particle collection characteristics of a single-stage dichotomous sampler. Environ Sci Technol. 12(6):679–682. https://doi.org/10.1021/es60142a006

Rao NP, Fernandez De La Mora J, McMurry PH. 1992. High-resolution aerodynamic spectrometry of submicron particles: sheathed variable-cut impactors vs other devices. J Aerosol Sci. 23(1):11–26. https://doi.org/10.1016/0021-8502(92)90314-l

Rao NP, Navascues J, Fernandez De La Mora J. 1993. Aerodynamic focusing of particles in viscous jets. J Aerosol Sci. 24(7):879–892. https://doi.org/10.1016/0021-8502(93)90068-k

Tsai CJ, Cheng YH. 1995. Solid particle collection characteristics on impaction surfaces of different designs. Aerosol Sci Technol. 23(1):96–106. https://doi.org/10.1080/02786829508965297

Tsai CJ et al. 2012. Novel active personal nanoparticle sampler for the exposure assessment of nanoparticles in workplaces. Environ Sci Technol. 46(8):4546–4552. https://doi.org/10.1021/es204580f[22435654]

Turner JR, Hering SV. 1987. Greased and oiled substrates as bounce-free impaction surfaces. J Aerosol Sci. 18(2): 215–224. https://doi.org/10.1016/0021-8502(87)90057-7

Vanderpool RW, Lundgren DA, Kerch PE. 1990. Design and calibration of an in-stack low-pressure impactor. Aerosol Sci Technol. 12(2):215–224. https://doi.org/10.1080/02786829008959341

Visser J. 1972. On Hamaker constants: a comparison between Hamaker constants and Lifshitz-van der Waals constants. Adv Colloid Interface Sci. 3(4):331–363. https://doi.org/10.1016/0001-8686(72)85001-2

Wang HC, Kasper G. 1991. Filtration efficiency of nanometer-size aerosol particles. J Aerosol Sci. 22(1):31–41. https://doi.org/10.1016/0021-8502(91)90091-u

Weir G, McGavin P. 2008. The coefficient of restitution for the idealized impact of a spherical, nano-scale particle on a rigid plane. Proc R Soc A. 464(2093):1295–1307. https://doi.org/10.1098/rspa.2007.0289